Control mechanisms for the global structure of scalar dispersion in chaotic flows

Daniel Lester*
CSIRO Mathematics, Informatics and Statistics, Box 56 Graham Rd, Highett Victoria 3190, Australia

Guy Metcalfe
CSIRO Materials Science & Engineering, Box 56 Graham Rd, Highett Victoria 3190, Australia

Murray Rudman
Dept. Mechanical and Aerospace Engineering, Monash University, Clayton South Victoria 3168, Australia
(Received 31 December 2013; published 14 August 2014)

Scalar dispersion has complex interactions between advection and diffusion that depend on the values of the scalar diffusivity and of the (possibly large) set of parameters controlling the flow. Using a spectral method which is three to four orders of magnitude faster than traditional methods, we calculate the fine-scale structure of the global solution space of the advection-diffusion equation for a physically realizable chaotic flow. The solution space is rich: spatial pattern locking, an order-disorder transition, and optima in dispersion rates that move discontinuously with Peclét number and boundary condition type are some of the discoveries. We uncover the mechanisms which control pattern locking and govern the global structure of dispersion across the parameter space and Peclét number spectrum.

DOI: 10.1103/PhysRevE.90.022908 PACS number(s): 89.75.Kd, 47.54.−r, 44.05.+e, 47.85.M−

I. INTRODUCTION

Dispersion of a passive scalar ϕ (heat, chemical species, etc.) is important in a variety of phenomena from epidemiology to geophysics and across length scales from the molecular to the celestial [1,2]. Transport of ϕ proceeds simultaneously through organized motion—a flow $\mathbf{v}(\chi)$—and through disorganized motion—molecular diffusion—vastly different modes and scales of transport. We write $\mathbf{v}(\chi)$ because the flow depends on a set of parameters χ, which govern the underlying symmetries and dynamics of the organizational template upon which disordered phenomena play out [3]. In any parametrized dynamical system an important and natural need is characterization of the major qualitative changes as these parameters vary. In the context of scalar dispersion, this raises the following natural question: what features of the underlying organized flow inform the behavior of dispersion throughout the flow parameter space?

For flows which admit chaotic advection for certain values of the flow parameters χ, it is well known that the nontrivial Lagrangian flow structure can impart complex distributions of the scalar ϕ, leading to accelerated dispersion and significantly altered transport dynamics. What is less well understood, however, is how transitions in the Lagrangian topology of the advection template from regular to chaotic dynamics impact dispersion dynamics across the flow parameter space? Moreover, having complete parametric solutions is crucial for transport optimization in chaotic flows or for the inverse problem of estimating parameter values from observations [4]. However, complete parametric solutions are difficult to compute due to the cost of evolving a solution for each point on a fine grid throughout a (possibly) large-dimensional parameter space.

In this paper we investigate how the properties of the underlying advection template govern the parametric distribution of scalar dispersion in regular and chaotic flows, across a range of time scales from diffusion-dominated to advection-dominated systems. We consider the global structure of transport of reoriented unidirectional duct flows as an example of the much larger class of flows which possess variable control parameters χ which govern the transition from regular to chaotic Lagrangian dynamics. Such reoriented duct flows are particularly relevant to continuous mixers (including microfluidic mixers and industrial mixers such as the Kenics mixer [5], SMX mixer [6], RAM mixer [7], and idealizations thereof) which consist of a uniaxial duct flow, upon which a systematically reoriented transverse flow is superposed. The flow control parameters χ govern both the reoriented transverse and uniaxial duct flows, and it is the interplay of these flows which lead to chaotic dynamics for particular values of χ. Whilst reoriented duct flows represent a subset of all chaotic flows, the mechanisms studied herein which control the global structure of scalar dispersion are universal to all flows, both regular and chaotic.

We first explore the global structure of scalar advection and mechanisms controlling the transition from regular to chaotic dynamics, and subsequently utilize these insights to understand those factors which control scalar dispersion. To obtain complete parametric solutions for scalar transport in a chaotic flow we utilize a composite spectral method which is three to four orders of magnitude faster than other methods of similar accuracy [8]. We then uncover the mechanisms which control the global structure of scalar dispersion across this parameter space and the relative time scales of advection and diffusion.

II. GLOBAL STRUCTURE OF SCALAR ADVECTION

Speetjens, Metcalfe, and Rudman [9] show that the general form of a duct flow subject to cellwise reoriented transverse forcing may be represented (in an appropriate frame of reference) as a piecewise constant flow in cylindrical coordinates

*daniel.lester@csiro.au

r, θ, z (with z the axial coordinate along the duct):

$$\mathbf{v}_{3D}(r,\theta,z) = v_z(r)\hat{\mathbf{e}}_z + \mathbf{v}_{r,\theta}\left(r,\theta - \Theta\left\lfloor \frac{z}{L} \right\rfloor\right), \qquad (1)$$

where v_z, $\mathbf{v}_{r,\theta}$ respectively are the axial and transverse flows, $\hat{\mathbf{e}}_z$ is the unit vector in the z direction, L is the axial length of each flow cell, Θ is the reorientation angle between cells, and $\lfloor x \rfloor$ is the floor function which represents the integer part of x. As such, reoriented duct flows may be idealized as a series of flow cells which are piecewise constant in z, with transverse flow reorientation occurring instantaneously at each cell boundary. Although in practice some degree of flow reorientation occurs at each cell boundary, the size and impact of this transition region is found to be small [7] for viscous-dominated flows relevant to mixing applications.

Due to their uniaxial nature, the Lagrangian topology of these incompressible three-dimensional (3D) steady duct flows is formally analogous to that of a time-dependent one degree-of-freedom Hamiltonian system [10], and the 3D steady advection-diffusion equation (ADE) governing scalar dispersion can also be transformed into an analogous transient 2D system under the assumption of negligible axial diffusion [11]. Hence the class of reoriented duct flows may be recast as a set of transient 2D flows of the form

$$\mathbf{v}_{2D}(r,\theta,t) = \frac{1}{v_z(r)}\mathbf{v}_{r,\theta}\left(r,\theta - \Theta\left\lfloor \frac{t}{\tau} \right\rfloor\right), \qquad (2)$$

by transforming the z coordinate into psuedotime t, which is regularized by the uniaxial flow $\mathbf{v}_z > 0$ for all r (ignoring the degenerate equilibrium points $\mathbf{v} = 0$ of measure zero on the duct boundary). As such, the Hamiltonian structure of advection in reoriented duct flows is clearly shown by the transform (2), which preserves the Lagrangian topology and associated symmetries. Furthermore, the 2D transient form serves as a convenient basis for visualization and elucidation of the global structure of dispersion. Henceforth in this study we use the 2D rotated arc mixing (RAM) flow shown in Fig. 1 (which is the 2D transient analog of the 3D steady RAM flow [7]) as an illustrative model flow which is representative of the class of all reoriented duct flows.

The 2D RAM flow confines fluid to a disk of radius R that has one boundary arc on which there is a constant tangential boundary velocity $R\Omega$; boundary velocity is zero outside this arc of opening angle Δ, shown here at $\pi/4$. Figure 1(b) shows the streamlines for this steady cavity flow $\bar{\mathbf{v}}(\mathbf{x})$. To generate chaotic particle orbits, the arc is displaced instantaneously through an angle Θ after every dimensionless time interval

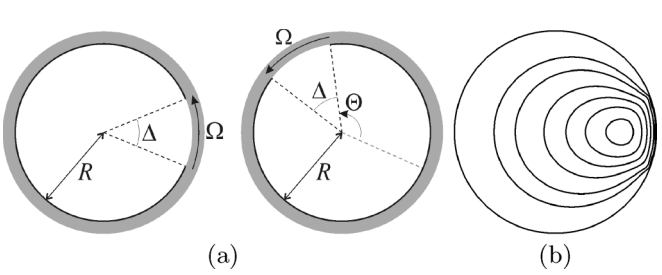

FIG. 1. Rotated arc mixer (RAM) flow (a) geometry and parameters; (b) streamlines for Newtonian Stokes flow [12].

$\tau = t\Omega$ to reorient the flow. In the limit of vanishing Reynolds and Strouhal numbers, the RAM flow can be considered as a piecewise steady flow comprised of the periodically reoriented base flow shown in Fig. 1(b):

$$\mathbf{v}(\mathbf{x},t) = \bar{\mathbf{v}}\left(r,\theta - \Theta\left\lfloor \frac{t}{\tau} \right\rfloor\right). \qquad (3)$$

Hence the 2D RAM flow parameters are $\chi = \{\tau,\Theta\}$; these parameters control the Lagrangian dynamics of the flow, which have been extensively studied [7,9]. Whilst the details of specific reoriented duct flows may vary, the parameters of reorientation angle and frequency are common to all such flows; hence the 2D RAM possess qualities which are generic to all reoriented duct flows. The RAM is one of many experimentally realizable chaotic flows; however, studies of such flows have not extensively explored their dispersion properties as a function of the control parameters.

For all reoriented duct flows, the time-dependant Hamiltonian $H(r,\theta,t)$ corresponds to the transient stream function $\psi(r,\theta,t) = \psi_0(r,\theta - \Theta\lfloor t/\tau \rfloor)$, where $\psi_0(r,\theta)$ is the stream function [12] of the steady flow shown in Fig. 1(b). In the limit $\tau \to 0$, the generally time-dependent Hamiltonian H coincides with the time-averaged steady Hamiltonian $\bar{H}$,

$$\bar{H} = \frac{1}{j\tau}\int_0^{j\tau} H(r,\theta,t)dt = \frac{1}{j}\sum_{i=1}^{j}\psi_0(r,\theta - i\Theta), \qquad (4)$$

for rational $\Theta/2\pi = p/j$ (with integers p, j), whereas for $\Theta/2\pi$ irrational, the time-averaged Hamiltonian is axis symmetric:

$$\bar{H} = \lim_{T\to\infty}\frac{1}{T}\int_0^T H(r,\theta,t)dt = \frac{1}{2\pi}\int_0^{2\pi}\psi_0(r,\theta)d\theta. \qquad (5)$$

In the limit $t \to 0$ the Hamiltonian system is completely integrable, consisting of nested islands defined by the level set of $\bar{H}$, which coincide with the Poincaré section for the steady flow. Isopleths of $\bar{H}$ (and hence the Poincaré section) are either axis symmetric for irrational $\Theta/2\pi$, or j-fold rotationally symmetric for rational $\Theta/2\pi = p/j$. The distribution of rational numbers is Cantor set along the $\tau \to 0$ axis. Breakdown of this integrable state is necessary for the attainment of chaotic advection, and the flow parameter τ controls the size of the perturbation away from the integrable state. For small but finite τ the weak transient perturbation away from $H = \bar{H}$ can lead to breakup of rational orbits and as $\tau \to 1$ total disintegration of the integrable state. Although integrable orbits break up at finite τ, symmetry locking of Poincaré sections for rational $\Theta/2\pi$ persists for finite τ, leading to symmetry-locked "tongues" similar to frequency-locked Arnol'd tongues [13]. These symmetry-locked tongues in (τ,Θ) space emanate from rational values of $\Theta/2\pi$ at the $\tau \to 0$ limit, and widen with increasing τ until they collide with neighboring tongues, where the competing resonances break the underlying symmetry, leading to a period-doubling route to chaos. This behavior is generic to all reoriented unidirectional duct flows.

The origin and persistence of symmetry locking in reoriented duct flows is revealed by consideration of the evolution of the offset angle ϕ between the material coordinate θ_m and

the forcing angle θ_f [14]:

$$\phi = \theta_m - \theta_f. \tag{6}$$

Symmetry locking occurs when the time average $\langle\phi\rangle$ of the offset angle is steady, corresponding to rotationally symmetric structures in the advection map. For an arbitrary offset angle Θ, the forcing relative to a rational angle $2\pi p/j$ in the neighborhood of Θ is

$$\theta_f = \left(2\pi\frac{p}{j} - \Theta\right)\lfloor t/\tau \rfloor, \tag{7}$$

whilst the material coordinate θ_m evolves as

$$\dot{\theta}_m = \mathcal{R}_{\Theta\lfloor\frac{t}{\tau}\rfloor}[\bar{v}_\theta(r,\theta)], \tag{8}$$

where $\bar{v}_\theta(r,\theta)$ is the angular velocity component of the steady duct flow $\bar{\mathbf{v}}(\mathbf{x})$. The time-averaged material coordinate evolves as

$$\langle\dot{\theta}_m\rangle \equiv \lim_{T\to\infty}\frac{1}{T}\int_0^T \mathcal{R}_{\Theta\lfloor\frac{t}{\tau}\rfloor}[\bar{v}_\theta(r,\theta_m)]dt, \tag{9}$$

which for a Fourier expansion in θ of $\bar{v}_\theta$ yields

$$\langle\dot{\theta}_m\rangle = \lim_{T\to\infty}\frac{1}{T}\int_0^T\left[a_0(r) + \sum_{k=1}^{\infty} a_k(r)\cos k\left(\theta_m + \Theta\left\lfloor\frac{t}{\tau}\right\rfloor\right)\right.$$
$$\left. + b_k(r)\sin k\left(\theta_m + \Theta\left\lfloor\frac{t}{\tau}\right\rfloor\right)\right]dt, \tag{10}$$

where $a_k(r)$, $b_k(r)$ are the (r-dependent) Fourier expansion coefficients. For base flows $\bar{\mathbf{v}}(\mathbf{x})$ which possess a reflection-reversal symmetry [such as the RAM base flow, Fig. 1(b) about $\theta = 0$], the sine coefficients b_k are zero. As the floor function may only take on integer values, and using (6), the integral (10) may be expressed as

$$\langle\dot{\theta}_m\rangle = \lim_{N\to\infty}\frac{1}{N}\sum_{n=1}^{N} a_0(r) + \sum_{k=1}^{\infty} a_k(r)\cos k\left(\phi + n2\pi\frac{p}{j}\right). \tag{11}$$

This sum admits a resonance condition, where the time-averaged contribution in (11) is nonzero only for wave numbers k which satisfy

$$k = mj, \tag{12}$$

for all integers $m > 0$. At resonance Eq. (11) simplifies to

$$\langle\dot{\theta}_m\rangle = \bar{\omega} + \sum_{m=1}^{\infty} a_{mj}(r)\cos(mj\phi), \tag{13}$$

where $\bar{\omega}$ is the areal average of $a_0(r)$. Hence the time-averaged locking variable ϕ evolves as

$$\langle\dot{\phi}\rangle = \langle\dot{\theta}_m\rangle - \langle\dot{\theta}_f\rangle$$
$$= \frac{\Theta - 2\pi\frac{p}{j}}{\tau} + \bar{\omega} + \sum_{m=1}^{\infty} a_{mj}(r)\cos(mj\phi), \tag{14}$$

which is of similar form to mode locking in the classic circle map which gives rise to Arnold tongues. Stable solutions of the locking equation (14) (corresponding to symmetry-locked regions with $\langle\phi\rangle$ steady) occur at values of ϕ for which $\langle\dot{\phi}\rangle = 0$ and $d\langle\dot{\phi}\rangle/d\phi < 0$, whilst unstable solutions correspond to $d\langle\dot{\phi}\rangle/d\phi > 0$. As $\langle\dot{\phi}\rangle$ is periodic in ϕ, Eq. (14) admits stable solutions under the condition

$$\left|\frac{\Theta - 2\pi\frac{p}{j}}{\tau} + \bar{\omega}\right| < A_j(r), \tag{15}$$

where $A_j(r)$ is the maximum value of $\sum_{m=1}^{\infty} a_{mj}(r)\cos(mj\phi)$ over $\phi \in [0,2\pi]$. As such, given control parameters Θ, τ, the fraction $f_{p,j}$ of j-fold symmetry-locked orbits which satisfy (15) is

$$f_{p,j}(\Theta,\tau) = \int_0^1 H\left(\left|\frac{\Theta - 2\pi\frac{p}{j}}{\tau} + \bar{\omega}\right| - A_j(r)\right)dr, \tag{16}$$

where H is the Heaviside step function.

The distribution of the fraction of locked orbits for the 2D RAM flow with $\Delta = \pi/4$ is shown in Fig. 2. Similar to frequency locking in Arnol'd tongues, the strength of symmetry locking decreases with the resonance j, such that low-j tongues dominate. For the 2D RAM flow $\bar{\omega} = -\Delta/(3\pi)$, and so the symmetry-locked tongues emanate from the $\tau = 0$ axis at an angle of $\arctan(-1/\bar{\omega}) = \arctan 12$. Hence the distribution of the fraction of symmetry-locked orbits (not accounting for symmetry breaking due to competing resonances) across the RAM flow parameter space is given by the sum

$$f(\Theta,\tau) = \min\left(1, \sum_{j=1}^{\infty}\sum_{p=1}^{j-1} f_{p,j}(\Theta,\tau)\right). \tag{17}$$

The distribution of locking intervals over the 2D RAM flow parameter space as predicted by (17) for $\Delta = \pi/4$ is illustrated in Fig. 3, where collision of the symmetry-locked tongues at $\tau \sim 1$ is clearly shown. The labeled points in Fig. 3 correspond to the Poincaré sections shown in Fig. 4, where (a), (b), (c) represent integrable solutions with $j = 2,3,4$-fold rotational symmetry, respectively, which lie on $\Theta = 2\pi p/j$ tongues. Figure 3 demonstrates that accumulation of symmetry-locked tongues does not occur at a single critical value of τ, but for $\tau \gtrsim 1$ symmetry breaking occurs due to competing resonances and the symmetry-locked integrable state is destroyed. The

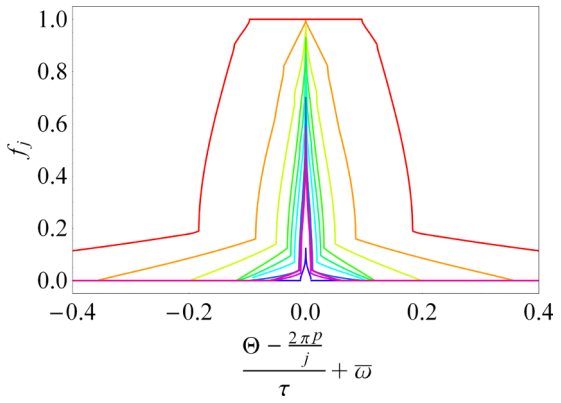

FIG. 2. (Color online) Distribution of the fraction f_j for $j = 1,2,\ldots,10$ (distributions narrow with increasing j) of locked orbits in the RAM flow as a function of flow parameters Θ and τ for locking angles $2\pi p/j$.

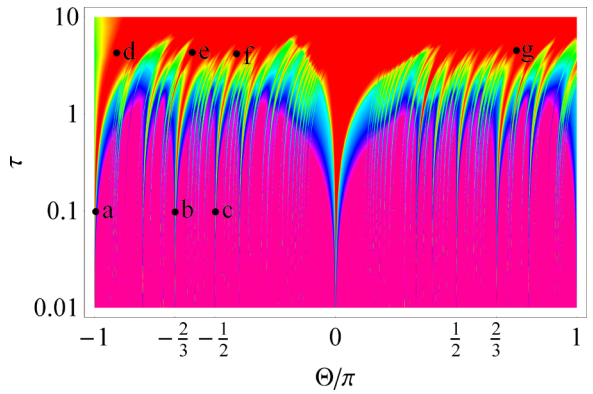

FIG. 3. (Color online) Map of the fraction $f(\Theta,\tau)$ of symmetry-locked orbits in the RAM flow parameter space $\mathcal{Q}$, ranging from $f = 0$ (pink) to $f = 1$ (red).

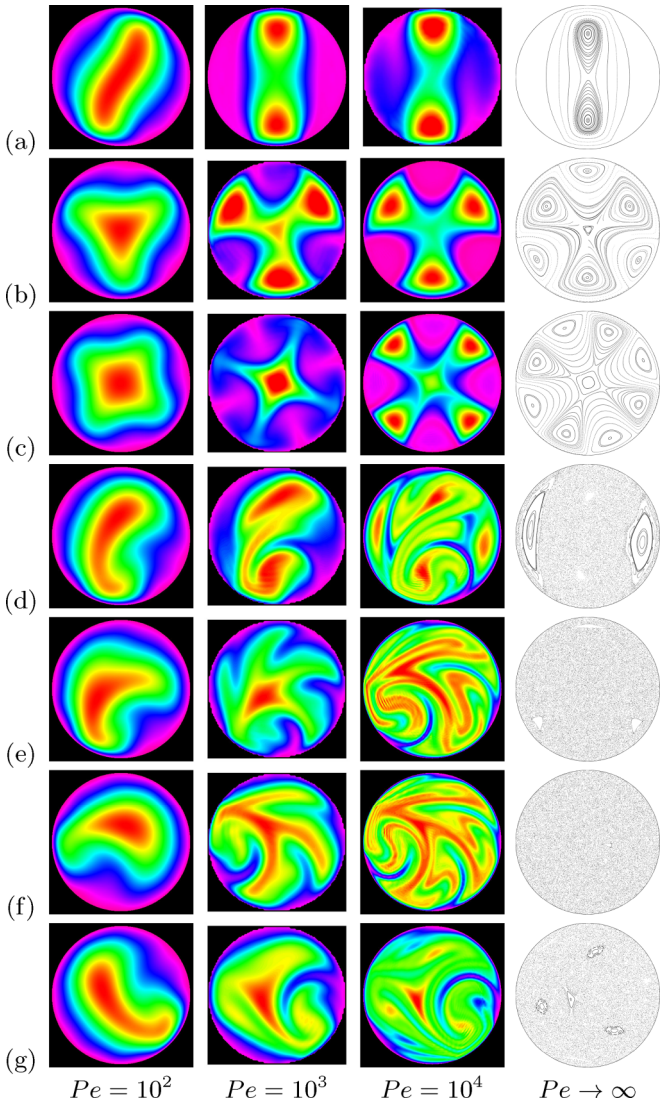

FIG. 4. (Color online) Dominant strange eigenmodes (finite Pe) and Poincaré sections (infinite Pe) for select points in the $\{\tau,\Theta\}$ plane.

route to chaos occurs via breakup of rational tori and a series of period-doubling bifurcations of elliptic points, leading to globally chaotic and nonhyperbolic Lagrangian topologies as shown in the Poincaré sections for points (d)–(g). Note that all topologies within the (τ,Θ) space inherit a reflection symmetry through the line $-\Theta/2$ which is a manifestation of the reflection-reversal symmetry of the 2D RAM base flow [9,14].

The transition from regular to chaotic dynamics with increasing τ is reflected in the map of stretching rates for the steady 3D RAM flow shown in [7]; here the stretching rate is zero for $\tau < \tau_{\text{crit}}(\Theta)$, and plateaus to a maximum upper bound for large τ away from $\Theta = 0$. Whilst the quantitative details of the global structure of scalar advection over the flow parameter space may vary for different reoriented duct flows, the qualitative picture of symmetry locking for rational values of $\Theta/2\pi$ at low τ which expand and eventually collide at higher τ to generate symmetry breaking and a route to chaos is generic to all reoriented unidirectional duct flows. As such, the global structure of scalar advection for reoriented duct flows is well understood, and forms the structural template for the organization of global dispersion.

III. GLOBAL STRUCTURE OF SCALAR DISPERSION

Dispersion of a passive scalar ϕ arises from the complex interactions between organized fluid motion (advection) and disordered molecular diffusion, leading to a dissipative dynamical system for the evolution of ϕ. As such, the advection dynamics provide an organizational template upon which dispersion plays out [1], and so the global structure of scalar advection informs the global structure of scalar dispersion. For the (generally unsteady) flow parametrized by χ, scalar dispersion is described by the advection-diffusion equation (ADE)

$$\frac{\partial\phi}{\partial t} + \mathbf{v}(\chi)\cdot\nabla\phi = \frac{1}{\text{Pe}}\nabla^2\phi, \tag{18}$$

subject to appropriate boundary and initial conditions. The Peclét number $\text{Pe} = LV/D$ reflects the relative time scales of advection and diffusion, where L, V are characteristic length and velocity scales, and D is molecular or thermal diffusivity. For the 2D RAM flow $\text{Pe} = R^2\Omega/D$, giving the dispersion parameter space as $\mathcal{Q} : \{\tau,\Theta,\text{Pe}\} = (0,\infty)\times[-\pi,\pi]\times[0,\infty)$. In general, the full parameter space of the ADE is $\mathcal{Q} : \chi\times\text{Pe}$, over which the qualitative and quantitative characteristics of ADE solutions can vary significantly, depending upon the nature of the advection dynamics considered in the previous section, and the relative timescales of advection and diffusion as quantified by Pe.

Studies have firmly established that fundamental solutions of the ADE are given by "strange eigenmodes"—sets of naturally persistent spatial patterns with decaying amplitude which arise as a consequence of the ADE admitting an inertial manifold to which all reasonable initial conditions are attracted. First reported from simulations with random velocity fields [15], strange eigenmodes have since been experimentally observed [16] and rigorously derived [17], and are so named due to the nontrivial spatial structure obtained in the singular limit $\text{Pe} \to \infty$.

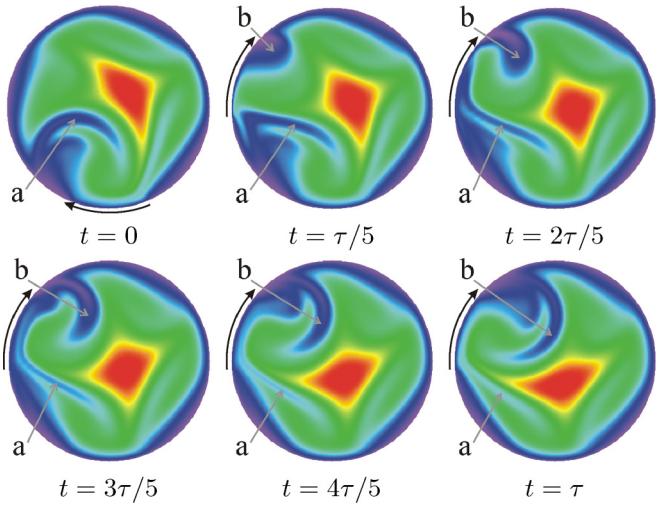

FIG. 5. (Color online) Persistence of a strange eigenmode (with decaying amplitude removed) through one reorientation interval. At $t = 0$ the moving boundary indicated by the arrow moves. Region (a) has been stretched and folded; diffusion heals the pattern along folds. Simultaneously advection stretches and makes new folds around the region (b). The pattern at τ persists, albeit rotated by Θ.

For time-periodic velocity fields, strange eigenmodes $\varphi_k(\mathbf{x},t)$ are Floquet modes of the advection-diffusion operator $\mathcal{L}_2[\varphi] = -\mathbf{v}\cdot\boldsymbol{\nabla}\varphi + \frac{1}{\mathrm{Pe}}\nabla^2\varphi$, and ϕ is composed of a finite sum of eigenmodes:

$$\phi(\mathbf{x},t) = \sum_{k=0}^{K} \alpha_k(t)\,\varphi_k(\mathbf{x},t)\,e^{\lambda_k t} \to \alpha_0(t)\,\varphi_0(\mathbf{x},t)\,e^{\lambda_0 t}, \quad (19)$$

where the sum is ordered by the magnitude of the real parts of the eigenvalues λ_k of $\mathcal{L}_2$, with initial weights $\alpha_k(0)$. The nonmodel (time-dependent) form of $\alpha_k(t)$ reflects the non-self-adjoint nature of (18) [18], and so with time scalar energy is transferred between modes in an irreversible cascade toward $k = 0$. This behavior, in concert with the fact that λ_k have negative real parts with $\mathrm{Re}(\lambda_k) \geqslant \mathrm{Re}(\lambda_{k+1})$ means that within finite time only the most slowly decaying eigenmode ($k = 0$) dominates. As such, the long-time dispersion rate is given by $\mathrm{Re}(\lambda_0)$, and the distribution of φ_0 and λ_0 over $\mathcal{Q}$ represents the complete parametric solution of asymptotic dispersion.

Figure 5 (and the video online in Supplemental Material [19]) illustrates the cooperation between advection and diffusion as the pattern evolves through one reorientation interval. Shown is the evolution of the dominant eigenmode over one period τ with the exponentially decaying amplitude scaled out. At $t = 0$ the boundary arc velocity indicated by the arrow moves. Region (a) has been stretched and folded during the previous interval, and during the subsequent interval diffusion "heals" the pattern along this fold. Simultaneously advection stretches and makes new folds around the region (b). The pattern at τ resumes its original shape, rotated by Θ. Diffusion heals the pattern wherever folds bring parts of the patterns close together, and folding appears to play a larger role in sustaining the pattern than normally credited.

To compare dispersion in the 2D RAM flow for Dirichlet boundary conditions over a range of Peclét numbers, we introduce the asymptotic transport rate

$$q \equiv \frac{\mathrm{Re}(\lambda_0)\mathrm{Pe}}{\alpha_{0,1}^2}, \quad (20)$$

where $\alpha_{0,1}^2/\mathrm{Pe}$ is the asymptotic diffusion rate in the unit disk, and $\alpha_{0,1}$ is the first zero of the zero-order Bessel function of the first kind. Hence q quantifies the relative acceleration of dispersion with respect to the reference case of diffusion only ($\mathbf{v} = 0$) in a disk for a fluid with fixed scalar diffusivity, such that Pe scales as $R\Omega$. Figure 6 shows a series of contour plots of q calculated over 1.2×10^5 points over the τ-Θ plane for $\mathrm{Pe} = 10^1$–10^5 under homogeneous Dirichet boundary conditions [20]. Previous studies of the ADE in chaotic flows have either used model flows that greatly simplified the projected advection operator [21,22] or, when aimed at optimization, have calculated solutions at $O(10^1)$ points in $\mathcal{Q}$ [23,24, loc. cit.]. Other fast methods, such as the matrix mapping method [25–27] involve some degree of numerical diffusion which differs from molecular diffusion and so do not fully quantify scalar transport at finite resolution. Figure 6 shows a complete parametric solution for scalar transport in a physically realizable chaotic flow. Several features deserve comment.

The gross structure of the distribution of q across (τ,Θ) space for all Pe in Fig. 6 corresponds with the fraction of symmetry-locked orbits for the advection map (Fig. 3), suggesting that the symmetry locking informs the strange eigenmodes for $\tau \lesssim 1$. Note that Fig. 3 only captures the overlapped symmetry-locking regions of (τ,Θ) space, and does not reflect symmetry breaking due to collision of tongues or the transition to chaotic dynamics for $\tau \gtrsim 1$. For the dispersion maps in Fig. 6, the symmetry-locked tongues arise as ridges in q for all Pe, which also emanate from the $\tau = 0$ axis at angle $\arctan(1/\bar{\omega}) = \arctan 12$ due to rotation of the 2D RAM flow with $\Delta = \pi/4$ (note the apparent "bending" of these tongues in Fig. 6 is due to the logarithmic scaling of the τ axis). Symmetry locking of the strange eigenmodes which reside on these tongues is illustrated in Figs. 4(a)–4(c), where the eigenmodes for $\mathrm{Pe} = 10^2$–10^4 inherit locking from the corresponding Poincaré sections (a)–(c) which essentially represent the singular limit $\mathrm{Pe} \to \infty$ of (18).

The strength of symmetry locking for j-fold symmetric tongues decreases with j (as per Figs. 2 and 3), and likewise the width of the tongues in the dispersion plots (Fig. 6) decreases with increasing j. For large j, both Poincaré sections and strange eigenmodes for all Pe approach an angularly uniform distribution, namely the dominant Bessel mode for the diffusion problem, and so the maximum dispersion rate on the tongues rapidly weakens to $q \to 1$ as $j \to \infty$, as is the case for irrational $\Theta/2\pi$. Conversely, q is large on the ridges of the low j dominant Arnol'd tongues, and there exists a value of j (denoted $j_{\max}$) at a given Pe for which q is maximum. As expected, the strength of the tongues increases with Pe as advection becomes more dominant, and $j_{\max}$ increases with Pe ($j_{\max} = 2,3,4,5$ for $\mathrm{Pe} = 10^2, 10^3, 10^4, 10^5$, respectively). Whilst symmetry locking of eigenmodes persists for all Pe, the location of optimal dispersion in the tongues depends upon the interplay of advection and diffusion—higher values of Pe can resolve smaller-scale structure (i.e., larger j), as reflected in Figs. 4(a)–4(c) for $\mathrm{Pe} = 10^2$–10^3. The width of the locking

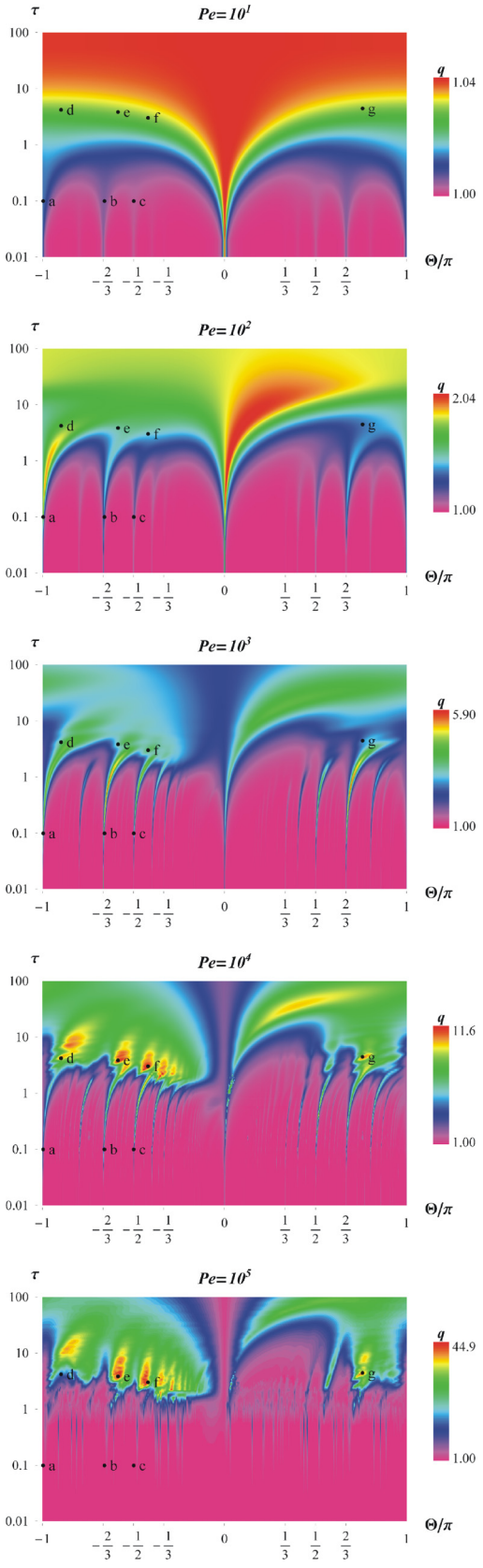

FIG. 6. (Color online) Map of the asymptotic transport rate $q \equiv \mathrm{Re}(\lambda_0)\mathrm{Pe}/\alpha_{0,1}^2$ for Dirichlet boundary conditions, $\Delta = \pi/4$ over the control parameter space $\mathcal{Q}$. Note the logarithmic scaling of q contours—different for each Pe—and the τ axis.

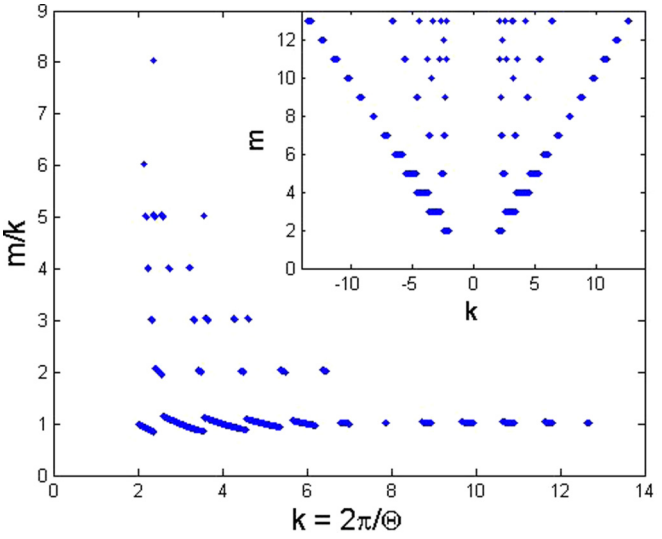

FIG. 7. (Color online) Symmetry-locked intervals of dominant strange eigenmodes in the RAM flow parameter space $\mathcal{Q}$. k is the wave number of the forcing and m is the azimuthal wave number of the pattern. Dots show the k intervals over which patterns are locked. (Inset) Locking is symmetric about $\Theta = 0$.

intervals for the dominant strange eignemodes in the 2D RAM flow is shown in Fig. 7, which correspond very well with the locking analysis in the previous section.

For $\tau \sim 1$, the mode-locked tongues in $\mathcal{Q}$ interact to produce an order-disorder transition, which breaks the symmetry of both the eigenmodes and underlying Poincaré sections. This mode breaking leads to chaotic advection dynamics for $\tau \gtrsim 1$, which corresponds to an order-disorder transition [see Figs. 4(e)–4(g)] for the strange eigenmodes within $\mathcal{Q}$. For $\mathrm{Pe} \gtrsim 10^3$, optimal dispersion occurs in the chaotic region of the parameter space $\mathcal{Q}$, whereas optima occur in ordered regions for $\mathrm{Pe} \lesssim 10^3$. The observation that optimal transport at low Pe occurs in regular flows may appear surprising; typically, coherent structures and regular regions (e.g., islands, KAM tori) in Poincaré sections are *barriers* to transport, and are expected to yield suboptimal transport. The points labeled (d)–(g) in Fig. 6 are disordered eigenmodes which corresponding to local optima in q. With decreasing Pe ($\lesssim 10^3$) these patterns are not sustainable due to "healing" of the eigenmode during evolution, as is clearly illustrated by the change in structure of eigenmodes (d)–(g) in Fig. 4 between $\mathrm{Pe} = 10^4$ and $\mathrm{Pe} = 10^3$. Note that at higher values of Pe (10^4–10^5), transport optima converge to fixed regions of the parameter space $\mathcal{Q}$ at values τ moderately higher than the order-disorder transition in which regions correspond to the optimum mixing regions of the flow [9] in the absence of diffusion. Whilst the dispersion results presented are those for the 2D RAM flow, the general structure of $\mathcal{Q}$ is generic to all reoriented duct flows, and furthermore the mechanisms governing dispersion persist for all advection-diffusion systems.

IV. MECHANISMS GOVERNING SCALAR DISPERSION

To uncover the mechanisms governing the global structure of the dispersion rate distribution q across $\mathcal{Q}$ in Figs. 6

and 4, we define the gradient variance of the dominant eigenmode $\|\overline{\nabla\varphi_0}\|^2$, where $\|\cdot\|$ and $\bar{\cdot}$ denote the L_2 norm and temporal averaging operations, respectively. Liu and Haller [17] show that for purely real (i.e., neither subharmonic nor quasiperiodic) eigenmodes

$$\lambda_0 = \frac{1}{\mathrm{Pe}}\frac{\|\nabla\bar{\varphi}_0\|^2}{\|\bar{\varphi}_0\|^2}, \tag{21}$$

and so scalar dispersion is governed by the distribution of the scalar gradient $\nabla\varphi_0$. We focus attention on the dominant eigenmode as this mode dictates scalar dispersion; the low variance of φ_0 (compared to φ_k for $k > 0$) ensures most of the initial data is mapped onto this mode, and furthermore the non-self-adjoint form of the ADE (18) imparts transfer of energy from higher modes toward φ_0 with time. Spectral expansion of the dominant eigenmode in terms of the Laplacian eigenfunctions $\omega_n(\mathbf{x})$ with eigenvalues $-\mu_n^2$ facilitates study of the distribution of scalar energy over different spatial scales

$$\varphi_0(\mathbf{x},t) = e^{\lambda_0 t}\sum_n^{\infty}\alpha_n(t)\omega_n(\mathbf{x}), \tag{22}$$

as each wave number μ_n is associated with the length scale μ_n^{-1}, and the spectrum $\alpha_1^2,\alpha_2^2,\ldots$ represents the distribution of scalar variance over length scales decreasing with n. As the variance and gradient variance respectively are $\sum_n \alpha_n^2$, $\sum_n \mu_n^2\alpha_n^2$, accelerated dispersion corresponds to maintenance of high wave-number modes in the distribution or, in physical space, the maintenance of small length scales. Substitution of (22) into (18) yields an equation for evolution of scalar variance

$$\frac{1}{2}\frac{d\alpha_n^2}{dt} = \sum_m H_{mn}(t)\alpha_n\alpha_m - \frac{\mu_n^2}{\mathrm{Pe}}\alpha_n^2, \tag{23}$$

where $H_{mn}(t)$ is the antisymmetric spectral advection operator. Accordingly, advection acts to increase gradient variance by the transfer of variance from small to large wave numbers (i.e., creation of striations via stretching and folding), whilst diffusion acts to remove variance as μ_n^2. Persistence of eigenmodes means that the transfer of variance must balance, and so it is the *creation* and *maintenance* of scalar variance in the dominant eigenmode which controls scalar dispersion. Whilst many flows can create high scalar variance, only those which maintain high variance in the dominant eigenmode generate significantly accelerated dispersion.

This is most clearly illustrated by the Batchelor scale $l = \sqrt{D/\gamma}$, which represents the minimum sustainable length scale (i.e., striation width) for a given stretching rate γ. From (23), the maximum sustainable wave number for a chaotic flow with constant uniform stretching field scales as $1/\sqrt{\mathrm{Pe}}$. Hence a moderate reduction in Pe can result in a dramatic reduction in transport rate, as reflected by the change in energy spectra (Fig. 8) for the mixing case (e) when Pe is reduced from 10^4 to 10^3—wave numbers $n \approx 2000$–3000 cannot be sustained at lower Pe, where the appearance of healing events significantly lowers the dispersion rate. Conversely, for the completely integrable cases [Figs. 4(a)–4(c)], the structure is only moderately altered between $\mathrm{Pe} = 10^3$ and $\mathrm{Pe} = 10^4$; in this case the Poincaré section contains large-scale structures which are robust with regard to changes in Pe.

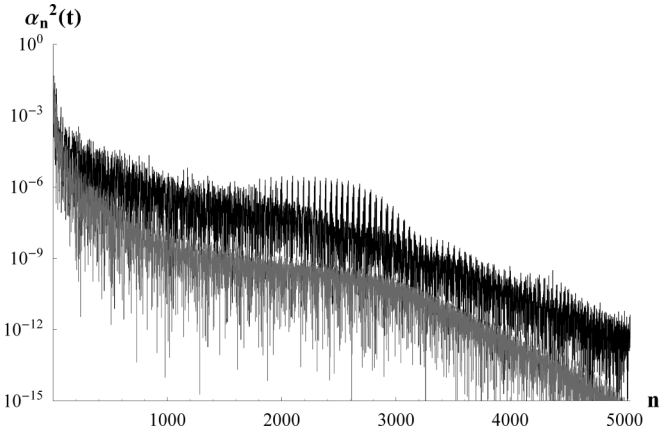

FIG. 8. Energy spectra for mixing protocol (e) at $\mathrm{Pe} = 10^4$ (black) and $\mathrm{Pe} = 10^3$ (gray).

By this reasoning, for all flows only low wave-number structures are sustainable at low Pe, and the maximum dispersion rate occurs for regular Lagrangian dynamics (e.g., the symmetry-locked tongues in Fig. 6); however, with increasing Pe higher wave-number structures are now sustainable (e.g., movement of optima into higher j-fold symmetric tongues in Fig. 6). In the diffusion-dominated regime, eigenmode structure (and hence dispersion rate) is informed by the integrable Poincaré section (as per Fig. 4). At greater values of Pe, a transition arises where optimum dispersion can now occur in the chaotic region of the flow parameter space [e.g., Figs. 4(d)–4(g)]. In this region, the scalar structure is no longer dictated by the gross structure of the Poincaré section, but rather is informed by the distribution of stretching histories, as quantified by the finite-time Lyapunov exponent (FTLE) $\nu(\xi,t)$ in Lagrangian coordinates ξ. Tang and Boozer [28] show that the structure of the FTLE field governs scalar dispersion, whereby the curvature of sharp ridges which define Lagrangian coherent structures (LCSs) [29] in the FTLE field act as barriers to transport, as well as the usual nonhyperbolic structures such as KAM tori (where $\nu = 0$). Hence the structure and dissipation rate of all eigenmodes are "programmed" by the FTLE distribution, as illustrated in Fig. 9.

The Poincaré section in Fig. 9(a) shows several small islands. Nested KAM surfaces are situated around a period 1 elliptic point at the 11 o'clock position, and at the 5 o'clock position a group of tori around a central island form an isolated mixing region which in the absence of diffusion does not exchange material with the surrounding fluid. Three periodic points also occur at the 11, 3, and 7 o'clock positions which are also associated with KAM tori and surrounding cantori. The FTLE distribution is shown in Fig. 9(b), where red and purple correspond to regions of zero and high stretch rate, respectively. There exists zero stretching within the integrable region of the domain and negligible stretching with the sticky stochastic layer surrounding KAM tori. Along with these topologically distinct regular regions, the LCSs shown in Fig. 9(c) form transport barriers which clearly inform all eigenmodes as per Figs. 9(d)–9(h). Most notably, strong LCSs

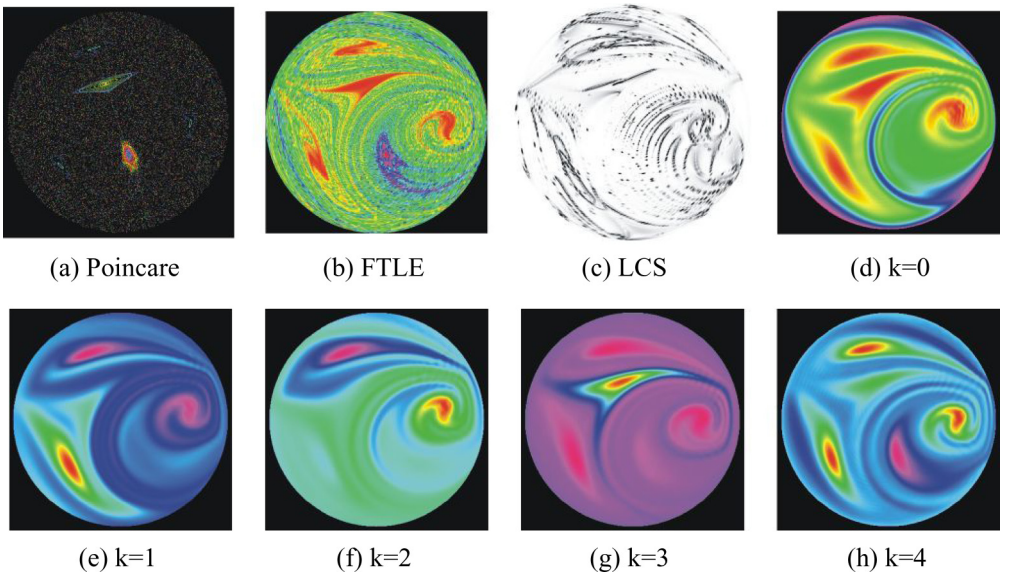

FIG. 9. (Color online) (a) Poincaré section, (b) finite-time Lyapunov exponent distribution, (c) barriers to diffusive transport, and (d)–(h) dominant five eigenmodes at Pe $= 10^4$, $\tau = 8$, $\Theta = 4\pi/5$, and $\Delta = \pi/4$.

correspond very well with large transverse scalar gradients in the eigenmodes.

The governing role of LCSs also explains the convergence of dispersion optima in $\mathcal{Q}$ at large Pe; with increasing Pe the optimum moves in $\mathcal{Q}$ as smaller and smaller striations are sustainable in the dominant eigenmode, until eventually the optimum mixing case (in the absence of diffusion) is sustainable. At this value of Pe (i.e., Pe $= 10^4$–10^5 in Fig. 6), the dispersion optima are localized to optimum mixing cases which are further refined with increasing Pe. As such, solution of the dispersion rate distribution q over the flow parameter space $\mathcal{Q}$ to high resolution for large (i.e., 10^4–10^5) Pe via the composite spectral method represents a highly efficient means of investigating both *dispersion* and *advective* mixing, especially compared to the computational cost of resolving this space to high resolution using, e.g., particle tracking methods.

V. CONCLUSIONS

Using the composite spectral method, we have calculated asymptotic solutions of the ADE for a chaotic flow over the global parameter space $\mathcal{Q}$ for a range of Peclét numbers Pe $= 10^1$–10^5 in terms of dominant strange eigenmodes $\varphi_0(\mathbf{x},t)$ and their associated dispersion rate λ_0. By composing the transient chaotic flow from a single steady velocity field to fully exploit the inherent symmetry of the RAM flow, this approach imparts significant numerical efficiency in exploration of the dispersion parameter space. The global structure of solutions over the parameter space is rich, exhibiting a fractal structure with spatial symmetry locking akin to Arnol'd tongues for quasiperiodic frequency locking, and an order-disorder transition in the eigenmodes around $\tau \sim 1$ as symmetry-locked tongues interact and resonances compete.

We show that this tongue structure is governed by symmetry locking of the underlying advection map, and derive the distribution of the fraction of locked orbits. This distribution agrees very well with the symmetry-locked structures for the dispersion problem, and the associated strange eigenmodes inherit modal symmetry from the advection map. At low values of Pe, dispersion optima arise on symmetry-locked tongues in the nonchaotic region of $\mathcal{Q}$, and with increasing Pe $\sim 10^3$ the dispersion optima transition to the chaotic region of $\mathcal{Q}$, and finally converge around Pe $\sim 10^5$ to localized regions which correspond to optimum mixing cases. This behavior is explained by the persistence of the dominant eigenmode, such that the optimum dispersion at any Pe is determined by the maximum sustainable scalar gradient within the dominant eigenmode. At low Pe, optimum eigenmodes are ordered and governed by the corresponding modally symmetric Poincaré section, whereas at higher Pe, chaotic flows generate sustainable eigenmodes with small-scale structure. In this regime, Lagrangian coherent structures (LCSs) of the flow form transport barriers which directly inform the structure of all eigenmodes.

Convergence of dispersion optima at high Pe indicates that the composite spectral method is an efficient means of determining both optimal dispersion and mixing across the entire flow parameter space, and this method can be applied to non-Newtonian and granular flows with velocities determined either numerically or experimentally, or to transport in turbulent flows if the temporal field is decomposed via, e.g., proper orthogonal decomposition. These results show that the global structure of dispersion is governed by the maximum sustainable scalar gradient within the dominant eigenmode, which at low Pe is determined by the gross structure of the integrable Poincaré section, and at high Pe Lagrangian coherent structures of the flow field.

APPENDIX

To construct many solutions of (18) over $\mathcal{Q}$ we utilize the composite spectral method [8] which expands ϕ and $\mathcal{L}_2$ in terms of basis functions $\omega_n(\mathbf{x})$ of the Laplacian operator $\mathcal{L}_1$, truncating the expansion at N terms, i.e.,

$\phi(\mathbf{x},t) \approx \sum_{n=0}^{N-1} \Phi_n(t)\omega_n(\mathbf{x})$. Whilst there exist a number of efficient methods [25,26] based upon the matrix mapping method to an approximate solution of the ADE (18), this method is exact up to the truncation N. The spectral representation of the ADE via the composite spectral method is

$$\frac{d\mathbf{\Phi}}{dt} = \left(\mathbf{H}(t) - \frac{1}{\mathrm{Pe}}\mathbf{D}\right)\cdot\mathbf{\Phi} = \mathbf{A}(t)\cdot\mathbf{\Phi}, \tag{A1}$$

where $\mathbf{\Phi}$ is the vector of expansion coefficients, $\mathbf{H}(t)$ is the spectral advection operator $\mathbf{v}(\chi)\cdot\nabla$, and $\mathbf{D}$ is the diagonal matrix of $\mathcal{L}_1$ eigenvalues. Advection transfers variance between wave numbers via $\mathbf{H}(t)$, reflecting the potential for chaotic flow to create small-scale structure; countervailing diffusion irreversibly removes variance via $\mathbf{D}$ at a rate that increases with wave number. As such, the persistence of strange eigenmodes in time-periodic flows arises from the balance of scalar energy flux generated by these processes over one flow period.

Evolution of the scalar field in (A1) is given by the fundamental matrix solution $\mathbf{S}(t)$, where $\mathbf{\Phi}(t) = \mathbf{S}(t)\mathbf{\Phi}(0)$, and so the spectral representation of the strange eigenmodes is given by the eigenvectors of $\mathbf{S}(t)$ over one flow period. The composite spectral method seeks to exploit any symmetries in the underlying flow field to significantly increase computational efficiency. Whilst in general symmetries are not present in all flows, they are present in many model and engineered flows, for instance, with periodic forcing (e.g., lid-driven cavity [30]) or reorientation (e.g., ridged micromixers [31]) of a small number of steady velocity fields to yield a large number of transient flows which vary markedly with χ. As shown below, such decomposition can lead to significant computational advantages.

In the case of the RAM flow, symmetries are given by the periodically reoriented flow field $\mathbf{v}(\mathbf{x},t;\chi)$, which for fixed Δ can be constructed from the steady flow $\bar{\mathbf{v}}$ [Fig. 1(b)]:

$$\mathbf{v}(\mathbf{x},t;\chi) = \mathcal{R}_{\Theta\lfloor\frac{t}{\tau}\rfloor}[\bar{\mathbf{v}}(\mathbf{x})], \tag{A2}$$

where $\mathcal{R}_\theta$ is the rotation operator and $\lfloor x\rfloor$ is the floor function which returns the integer part of x. Hence the fundamental matrix solution $\mathbf{S}(t;\mathcal{Q})$ for the RAM flow at integer multiples of τ then is a product of the solution matrix for each of the q orientations in τ:

$$\mathbf{S}(n\tau;\mathcal{Q}) = \prod_{i=1}^{n}\mathbf{R}_{i\Theta}\cdot\exp(\bar{\mathbf{A}}\tau)\cdot\mathbf{R}_{i\Theta}^{-1} = [\mathbf{R}_\Theta\cdot\exp(\bar{\mathbf{A}}\tau)]^n, \tag{A3}$$

where $\mathbf{R}_\theta$ is the rotation operator matrix and $\bar{\mathbf{A}}$ is calculated from the steady flow $\bar{\mathbf{v}}$ via (A1). In a frame rotating with the window opening, the RAM flow is periodic with τ, and so the fundamental matrix solution in this frame is then $\mathbf{S}(\tau;\mathcal{Q}) = \mathbf{R}_\Theta\cdot\exp(\bar{\mathbf{A}}\tau)$, facilitating direct calculation of eigenmodes in this frame for window offset angles Θ which are irrational with respect to π. As many of the leading strange eigenmodes as desired are then calculated from the dominant eigenvectors of (A3) using the Arnoldi method.

[1] G. Metcalfe, M. Speetjens, D. Lester, and H. Clercx, in *Advances in Applied Mechanics*, Advances in Applied Mechanics Vol. 45, edited by E. van der Giessen and H. Aref (Elsevier, Amsterdam, 2012), pp. 109–188.

[2] T. Tél, A. de Moura, C. Grebogi, and G. Károlyi, Phys. Rep. **413**, 91 (2005).

[3] For example, in a Couette flow χ is the inner and outer cylinder radii and rotation rates, and aspect ratio; industrial processes have design, operating, and rheology parameters.

[4] *Research in Fluid Dynamics: Meeting National Needs*, edited by J. Gollub (U.S. National Committee on Theoretical and Applied Mechanics, www.usnctam.org, 2006).

[5] M. K. Singh, T. G. Kang, P. D. Anderson, H. E. H. Meijer, and A. N. Hrymak, AIChE J. **55**, 2208 (2009).

[6] M. K. Singh, P. D. Anderson, and H. E. H. Meijer, Macromol. Rapid Commun. **30**, 362 (2009).

[7] G. Metcalfe, M. Rudman, A. Brydon, L. Graham, and R. Hamilton, AIChE J. **52**, 9 (2006).

[8] D. R. Lester, M. Rudman, G. Metcalfe, and H. M. Blackburn, J. Comput. Phys. **227**, 3032 (2008).

[9] M. Speetjens, G. Metcalfe, and M. Rudman, Phys. Fluids **18**, 103103 (2006).

[10] K. Bajer, Chaos, Solitons & Fractals **4**, 895 (1994).

[11] D. R. Lester, M. Rudman, and G. Metcalfe, Int. J. Heat Mass Transfer **52**, 655 (2009).

[12] T.-H. Hwu, D.-L. Young, and Y.-Y. Chen, J. Eng. Mech. **123**, 774 (1997).

[13] J. A. Glazier and A. Libchaber, IEEE Trans. Circuits Syst. **35**, 790 (1988).

[14] G. Metcalfe, in *Complex Physical, Biophysical, and Econophysical Systems*, Lecture Notes in Complex Systems, edited by R. Dewar and F. Detering (World Scientific, Singapore, 2010), pp. 189–242.

[15] R. T. Pierrehumbert, Chaos, Solitons & Fractals **4**, 1091 (1994).

[16] D. Rothstein, E. Henry, and J. P. Gollub, Nature (London) **401**, 770 (1999).

[17] W. Liu and G. Haller, Physica D **188**, 1 (2004).

[18] P. J. Schmid, Annu. Rev. Fluid Mech. **39**, 129 (2007).

[19] See Supplemental Material at http://link.aps.org/supplemental/10.1103/PhysRevE.90.022908 for video of the evolution of the pattern of Fig. 5.

[20] Calculation of λ_0 and φ_0 for the 1.2×10^5 points in each plot in Fig. 6 took about 1.05×10^6 s on an Intel Xeon 3.00 Ghz CPU. To similar accuracy with a finite volume method (and analytic velocity), a *single* value of λ_0 from the evolution of ϕ took 5.1×10^4 s on the same machine, giving, in this case, about a $6000\times$ speedup for parametric solution; there is a larger speedup at higher Pe.

[21] S. Cerbelli, A. Adrover, and M. Giona, Phys. Lett. A **312**, 355 (2003).

[22] V. Toussaint, P. Carriere, J. Scott, and J. Gence, Phys. Fluids **12**, 2834 (2000).

[23] V. Ganesan, M. D. Bryden, and H. Brenner, Phys. Fluids **9**, 1296 (1997).

[24] A. J. S. Rodrigo, J. P. B. Mota, A. Lefèvre, and E. Saatdjian, Phys. Fluids **15**, 1505 (2003).

[25] O. Gorodetskyi, M. F. Speetjens, P. D. Anderson, and M. Giona, AIChE J. **60**, 387 (2014).

[26] C. P. Schlick, I. C. Christov, P. B. Umbanhowar, J. M. Ottino, and R. M. Lueptow, Phys. Fluids **25**, 052102 (2013).
[27] M. K. Singh, M. F. M. Speetjens, and P. D. Anderson, Phys. Fluids **21**, 093601 (2009).
[28] X. Z. Tang and A. H. Boozer, Phys. Fluids **11**, 1418 (1999).
[29] G. Haller, Physica D: Nonlin. Phenom. **240**, 574 (2011).
[30] J. M. Ottino, *The Kinematics of Mixing: Stretching, Chaos, and Transport* (Cambridge University Press, Cambridge, UK, 1989).
[31] A. Stroock, S. Dertinger, A. Ajdari, I. Mezíc, H. Stone, and G. Whitesides, Science **295**, 647 (2002).